MRI for Non-invasive thermometry

E. M. Kardoulaki, R. R. A Syms and I.R Young
EEE Dept., Imperial College London, Exhibition Road, London SW7 2AZ, UK
*TEL +44-207-594-6203 FAX +44-207-594-6308 Email ek03@ic.ac.uk

Introduction

Most of the magnetic resonance (MR) parameters that contribute to the signal intensity and phase exhibit temperature dependence. MRI has therefore been long attractive as a tool for non-invasive thermometry during thermal treatment of deep-seated organs. Real-time temperature mapping can ensure the thermal dose delivered is sufficient to cause damage to the target tissue volume only, and can provide feedback to adjust the thermal dose automatically. However, although the concept quickly matured into clinical use, the technique still suffers from problems that were identified early on [1,2], at least in-vivo.

The most extensively explored application of MR-thermometry today is the guidance of thermal therapies [3–26], where a series of temperature maps is acquired in close to real-time, to monitor the tissue being treated and its margins. The aim is less often to sensitize the tissue to radiotherapy or chemotherapy and more often to cause necrosis, typically by delivering but occasionally by abducting heat. Heat-based thermal treatments are separated into hyperthermia (involving temperature rises < 45 ºC, over several minutes) or ablation (50-80 ºC, over several seconds) depending on the temperature ranges and their time scales.

Approximately 40 medical centres worldwide routinely carry out MR-guided thermal treatments when surgical resection is not an option, or has been shown to be less effective [27]. Thermal energy is delivered via a high power laser source coupled to a fibre, usually inserted into the tissue in a minimally invasive way [14], delivered via a high intensity focused ultrasound (HIFU) system [7] or a hyperthermia unit [12], in a non-invasive way, or with an interstitial US [5], radio-frequency (RF) [28] or microwave probe [29], again minimally invasively. Laser and US sources are preferably used in conjunction with MRI.

The most commonly treated tissue is the liver; however with advances in equipment for delivery of thermal energy [5,7,11,14,28,30–32], accurate temperature monitoring, image reconstruction and automation [3,4,6,8,9,11–13,15–17,23–25,33-111], the possibilities are expanding. Emerging applications include local drug-delivery [112–114], epilepsy treatment [9], quality control of red blood cells [115], iron mapping [116], diagnosis of multiple sclerosis [117], and brain abnormalities [118,119] and identification of iron-oxide labelled stem cells [120].

Many different commercial systems exist [5,9,12,14,15,33,34,121–123] and Figures 1-4 show examples from clinical practise using state-of-the-art technology. Figure 1 shows images from a minimally invasive MR-guided liver laser interstitial thermal therapy (LITT) carried out at St. Mary's Hospital, London, indicating a) the radiofrequency (RF) coil (8-element HD cardiac) used for MR-guidance, and b) an example case of a lesion exceeding 2 cm diameter which required two ablations.

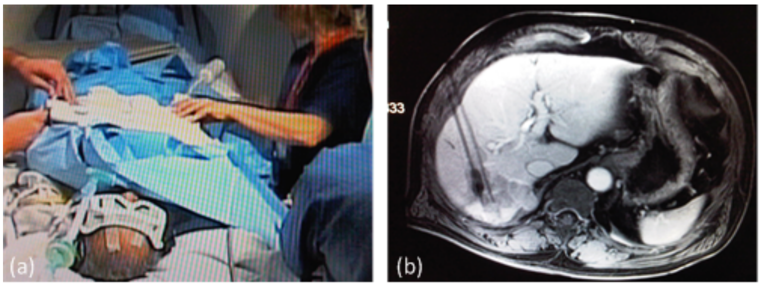

Figure 1 Liver LITT carried out at St. Mary's Hospital, London, UK: a) patient in the MR-suite, b) axial slice MRI showing a partially ablated lesion (images by kind permission of Prof. W.M.W Gedroyc, St. Mary's Hospital).

Figure 2 shows a system for transurethral prostate ultrasound ablation (TULSA-PRO, Profound Medical). It includes proprietary software for monitoring and temperature feedback control of the heating pattern. It has been used to treat 30 patients in a Phase I study at the University Hospital of Heidelberg (Germany), Western University (Canada) and William Beaumont Hospital (US) [5]. Figure 3 shows a HIFU system recently trialled on ten patients in the University Hospital of Utrecht, Netherlands [7]. It consists of electronically steerable transducers and an integrated RF receiver.

Figure 4 shows the non-invasive hyperthermia system BSD-2000 3D MRI (Pyrexar Medical) used to treat various types of cancer (e.g. rectal, bladder, ovarian, soft tissue sarcoma, cervical and pancreatic). The hyperthermia unit is a phased array of dipoles with filters to minimize RF interference. MR-guidance is performed through the SigmaVision®Advanced software (Dr. Sennewald Medizintechnik GmbH).

The aim here is to discuss the principles of operation of thermometry based on temperature-sensitive MR-parameters, to comment on the limitations and report on recent progress. Emphasis is placed on the potential of thin-film catheter-based RF coil technology to improve the MR-thermometry and the outcomes of MR-guided thermal treatments in general. We conclude with a general outlook for the field and comment on the possibility for future advances.

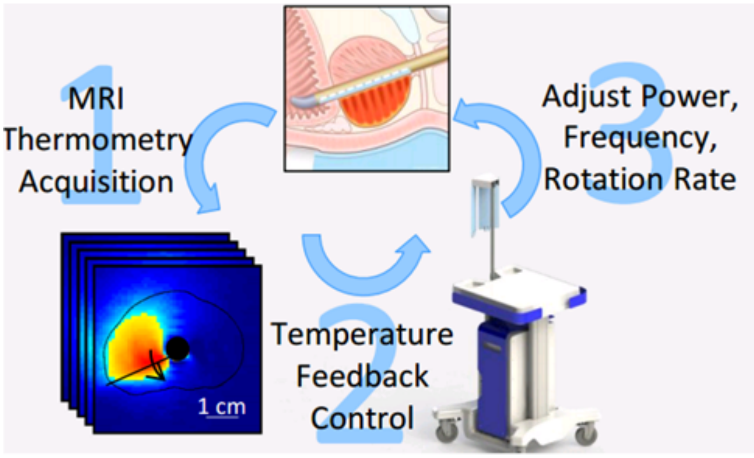

Figure 2 MR-guided ultrasound ablation of prostate cancer using the TULSA-PRO ten-element urethral device and a rectal cooling device. The feedback steps involved in the automated MR-guided procedure are illustrated (image by kind permission from Profound Medical Inc.)

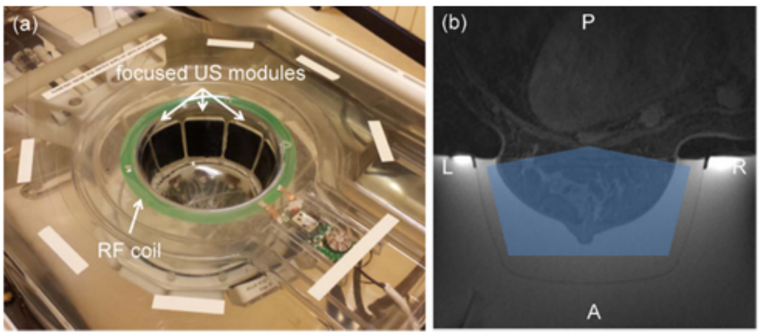

Figure 3 a) Breast MR-HIFU system showing the transducer elements surrounding the breast cap and the integrated RF receive coil, b) corresponding MR image indicating the region where focal point can be formed (image by kind permission from [7]).

Figure 4 MRI hyperthermia suite in the Erasmus Medical Centre (Rotterdam, Netherlands) consisting of the control and MRI rooms equipped with the BSD-2000 hyperthermia system (Pyrexar Medical); Illustration of the treatment control through the SigmaVision®Advanced software (Dr. Sennewald Medizintechnik), (image by kind permission from Pyrexar Medical and Dr. Sennewald Medizintechnik).

Temperature-sensitive MR-parameters

MR-thermometry is made possible by the intrinsic sensitivity to absolute temperature T of MR-parameters such as the electron screening constant of the water proton $\sigma(T)$, the proton density $M_0(T)$, the longitudinal relaxation time $T_1(T)$, the transverse relaxation time $T_2(T)$, the diffusion coefficient $D(T)$ and processes such as magnetization transfer.

T_1, T_2, and M_0 are accessed through the magnitude of the MR signal while the electron screening constant of ^{1}H is accessed by high resolution spectroscopy or indirectly by monitoring temperature induced phase changes in images acquired with a gradient recalled echo (GRE) sequence. These methods provide a temperature measurement, relative to a baseline with the exception of the proton resonance frequency spectroscopic methods, which can in theory provide an absolute temperature [53,84,119,124,125].

Most of the work has focused on exploiting the thermal dependency of T_1 and σ and MR-thermometry methods based on these are clinically accepted and routinely used. The extraction of temperature information through the magnitude signal initially gained popularity faster than proton resonance frequency methods, probably due to its simplicity. However, very soon, it was realized that the technique is not suitable for accurate quantitative measurements. Methods based on D, M_0 and T_2 have been significantly less popular. Here we focus on recent progress, while other excellent reviews can be found in [1,2,95,127].

T_1, T_2 and proton density

The magnitude of the NMR signal is proportional to the nuclear magnetization M_0 but also depends on the relaxation times T_1 and T_2 in a fashion determined by the parameters of the acquisition method in use (the repetition time TR, the echo time TE, and the flip angle α). For a spin-echo pulse sequence, the magnitude of the signal S for $\alpha = \pi/2$ can be described as:

$$S(TE,\ TR,\ T) = M_0(T)\ exp\left[-\frac{TE}{T_2(T)}\right]\left(1-exp\left[-\frac{TR}{T_1(T)}\right]\right) \tag{1}$$

The equilibrium of nuclei with spin 1/2 in a thermal bath and a magnetic field B_0 is governed by Boltzmann's distribution which predicts that the equilibrium nuclear magnetization M_0 is:

$$M_0 = \frac{N\gamma^2 h^2 I(I+1)B_0}{3\mu_0 k_B T} \tag{2}$$

where N is the number of spins per unit volume, γ is the gyromagnetic ratio, h is Planck's constant, I is the spin quantum number, B_0 is the static magnetic field, k_B is Boltzmann's constant and μ_0 is the permeability of free space. M_0 can be written in terms of the susceptibility χ_o, as $M_0 = \chi_o(T)\ B_0$, where χ_o follows the well-known Curie Law:

$$\chi_o \propto 1/T \tag{3}$$

M_0 has a small thermal coefficient of -0.3 %/ºC between 37 and 80 ºC [128]. The temperature dependence of T_1 was first observed by Bloembergen in 1948 [129]. It results from the changes in the dipolar interactions of macromolecules with temperature that follow the temperature–dependent changes in their translational and rotational motion. T_1 is expected to increase with temperature, and its temperature dependence can be described as:

$$T_1 \propto exp\left[-\frac{E_a(T_1)}{k_B T}\right] \tag{4}$$

where $E_a(T_1)$ is the activation energy of the relaxation process. Temperature-dependent transient changes in T_1 can be calculated for a small range of temperatures, relative to a reference value obtained at a baseline temperature T_b, as:

$$T_1\left\{T(t)\right\} = T_1\left(T_b\right) + b\left\{T(t) - T_b\right\} \tag{5}$$

Here b is the temperature coefficient dT_1/dT, which must be derived individually for the given subject and tissue-type undergoing thermal treatment.

The usual method of extracting T_1 is to ignore the smaller temperature-dependence of T_2 and acquire an image with a spin-echo or a GRE sequence with a short TE and a long TR for use as reference, and then follow this by obtaining an image with the same TE but a short TR. Equations (1) and (2) then imply that the signals from the two images are related by:

$$S / S_{ref} = \left(T / T_{ref}\right) \frac{1 - exp\left[-\dfrac{TR}{T_1\left(T\right)}\right]}{1 - exp\left[-\dfrac{TR}{T_1\left(T_{ref}\right)}\right]} \tag{6}$$

Most often, however, the temperature dependence of T_1 is considered only qualitatively, via measurements of the difference of the signal magnitude in the nth image and that acquired at T_b [3,26]. The signal is expected to decrease with increasing temperature, because T_1 will increase and M_0 will decrease following (3). Considering the signal difference and neglecting the temperature-dependence of other parameters and the dynamic effects can lead to significant errors in-vivo. It has been shown [130] that if $M_0(T)$ is ignored, then dT_1/dT will deviate from the theoretically expected value of 1% /°C, leading to a serious error.

T_2* increases approximately linearly as tissue temperature decreases below 0 ^{0}C [79,131,132]. Consequently, temperature mapping based on T_2* or the magnitude signal on T_2-weighted images has been recognised mainly for its potential during cryoablations [79,133]. Tables 1 and 2 summarize the values of the thermal coefficients of T_1 and T_2 respectively that have been measured for various tissues in published calibration experiments.

Table 1. Temperature coefficient of T_1 for different tissue types.

	[ms/ºC]	[%/ºC]	Range [ºC]	B_0 [T]
Human breast tissue [55]	8	2	n/a	n/a
Cortical bovine bone [70]	0.67-0.84	n/a	25 - 70	3
Human brain [71]	17.4 (cortex), 3.4 (white matter)	n/a	4-37	3
Human breast tissue [74]*	5.35 (at 25ºC) & 9.5 (at 65ºC)	n/a	25-65	1.5
Porcine fatty acids CH_2/CH_3 [81]**	10.7/30.3	1.69/3	20-60	11
Cortical bovine bone [134] ***	n/a	0.68-1.07	25-60	3
Bovine muscle [135]	n/a	1.4	10-40	1.5
Porcine liver [136]	n/a	1-2	10 – 50	1.5
Porcine fat [137]	3.9-7.7	n/a	30-70	1.5

* Reversible beyond 65ºC, Temperature error 2- 4 ºC, Water suppression applied
** Reversible, No hysteresis
*** Estimation via signal change, Fatty marrow was removed and fat suppression omitted

Table 2. Temperature coefficient of T_2 for different tissue types.

	[ms/ºC]	Range [ºC]	B_0 [T]
Cortical bovine bone [70]	0.67-0.84	25 - 70	3
Human brain [71]	Negligible	4-37	3
Human breast fat [74]	0.9	25-65	1.5
Porcine fatty acids CH_2/CH_3 [81]	11/22.3	20 -60	11
Porcine fat [138] *	5.17	25-74	1.5
Porcine fat /bovine marrow [139]**	6.1 – 6.4 / 7	25 -70	3

* Temperature accuracy of 0.9 ºC, reversible changes during cooling,
Relatively slow (16 s) acquisition; without water suppression dT_2/dT = 3.77 ms/ºC
**Irreversible changes beyond 45 ºC, Hysteresis;
Without water suppression dT_2/dT = 4.64 - 5.45 ms/ºC

Chemical shift of water proton

As the temperature of aqueous tissue changes, so do the nature and local number of hydrogen bonds. Variations in the hydrogen-bonding network affect the local magnetic field B_{loc} experienced by protons and changes thereof in turn proportionally shift their resonance frequency ω_L according to the Larmor equation:

$$\omega_L\left(T\right) = \gamma B_{loc} = \gamma B_0\left(1 - \sigma\left(T\right)\right) \tag{7}$$

Here B_{loc} is the local field the nucleus of the hydrogen atoms experience. The temperature-dependent electron screening constant $\sigma(T)$ is an indication of the shielding effect caused by the currents induced in the electron cloud. As temperature rises and the hydrogen bonds are disrupted, the shielding from the main magnetic field B_0 becomes more effective, leading to a decrease in the resonant frequency.

A change in the proton resonance frequency (PRF) therefore reflects temperature-induced changes in the chemistry of the microscopic environment of the H^1 nucleus. The electron screening constant is linearly related to temperature for the temperature range of interest for thermal ablations (-15 ºC to 100 ºC) and is independent of tissue type (with the exception of fat, for which $d\sigma_F/dT \approx 0$) [140]. Typically, it follows:

$$\sigma(T) = aT \tag{8}$$

Hindman [141] first demonstrated temperature measurements based on the chemical shift of water. He observed a very small effect for pure water, of the order of -0.0108 ppm/ºC. A list of in-vivo and ex-vivo tissue calibration studies is given in [142], indicating only a slight variation across different tissue types (between -0.007 and -0.01 ppm/ºC). MR-thermometry based on the water PRF shift was initially investigated using spectroscopic techniques and regained attention in-vivo only after Ishihara et al. [143] proposed a simple method of obtaining temperature information by observing phase differences in the image data acquired with a GRE sequence. PRF MR-thermometry has therefore evolved into two techniques: phase mapping and spectroscopic imaging.

Based on the phase mapping approach, the temperature of water relative to a baseline temperature T_b can be determined using:

$$T - T_b = \frac{\varphi(T) - \varphi(T_b)}{\gamma a B_0 TE} \tag{9}$$

where $\phi(T)$ is the phase in the n^{th} image during the thermal therapy, $\phi(T_b)$ is the phase in the baseline image acquired at the start and TE is the echo time of the GRE sequence. Spectroscopic imaging makes use of the temperature insensitivity of the electron screening constant of an internal reference peak such as a lipid or N-acetyl-aspartate (NAA), and could, in theory derive an absolute temperature based on a measurement of the frequency of the water resonance relative to the reference peak.

Based on (7), the PRF for water is $\omega_w(T) = \gamma B_0\{1 - \sigma_W(T)\}$, while the PRF of the temperature insensitive reference compound is $\omega_R = \gamma B_0(1 - \sigma_R)$. The temperature-dependent chemical shift of water can therefore be determined as:

$$\delta_{W-R}(T)\ [ppm] = [\{\omega_w(T)\ -\ \omega_R\}/\ \omega_{RF}]\ x\ 10^6 = \{\sigma_R - \sigma_W(T)\}\ x\ 10^6 \qquad (10)$$

where $\omega_{RF} \approx \gamma B_0$ is the Larmor frequency. The absolute temperature can then in principle be derived, as T(t) = ($\sigma_{W\text{-}R}$/a) + c, where a [ppm/ºC] is the temperature coefficient and c [ºC] is the temperature at which the chemical shift becomes zero.

Unfortunately (10) is not accurate in practice, because the tissue susceptibility $\chi(T)$ (which is also temperature-dependent) has been ignored. Including the susceptibility, the expression for the water PRF becomes $\omega_w(T) = \gamma B_0\{1 - \sigma_W(T) + \chi_W(T)\}$ and that of the reference compound now becomes temperature dependent, as $\omega_R(T) = \gamma B_0\{1 - \sigma_R + \chi_R(T)\}$. The impact of the susceptibility is often neglected although doing so can lead to temperature errors. This is discussed in detail in the following section.

Diffusion coefficient

The temperature-dependence of the diffusion coefficient was first demonstrated by Le Bihan [144] who showed a thermal sensitivity of 2.2 %/ºC. The relationship between the diffusion coefficient and temperature can be expressed as:

$$D(T)\ =\ exp\left[-\frac{E_a(D)}{k_B T}\right] \qquad (11)$$

Here $E_a(D)$ is the activation energy of the molecular diffusion of water and D is the diffusion coefficient [mm^2/s] which is determined for an applied diffusion weighting b (s/mm^2), as ln(S/S_0)/b, where S and S_0 are the voxel signal intensities in diffusion-weighted and reference (b = 0) images respectively. The thermal coefficient for small variations of E_a is then:

$$dD\ /\ dT = \frac{DE_a}{k_B T^2} \qquad (12)$$

A relative temperature difference can then be derived from two diffusion-weighted images, where one of them serves as a reference at the baseline temperature, as:

$$\Delta T\ =\ \left(\frac{k_B T_b^{\ 2}}{E}\right)\frac{D\ -\ D_b}{D_b} \qquad (13)$$

Limitations and recent progress

MR-thermometry has its limitations whichever of the parameters discussed above is used. The optimum choice typically depends on the particular application, which will determine the required speed of measurement, temperature accuracy and resolution. For thermal therapies, the organ being treated, the type of ablation (cryotherapy, LITT, or HIFU), the magnetic field strength, the hardware used (receiver coils), and the type of sequence all affect the performance with variations expected across different patients in the same type of tissue and treated at the same centre.

Limitations in methods based on the temperature-dependence of T_1, T_2 and proton density

Magnitude signal changes are caused by the combined effects of the temperature dependence of T_1, T_2 and M_0 and the dynamic alterations in the physiological response of tissue to heat (which affect all of these parameters) [74]. These effects cannot be easily decoupled. As the temperature starts to change, the body responds by increasing perfusion. Blood has a different density of MR-visible protons, different relaxation times and different susceptibilities as it degrades in an un-predictable way into its by-products [71,116]. The body also responds to stress by oedema which again affects the visible protons and their time constants [130,145].

The level and state of the water in the tissue also varies widely and the situation is even more complex in tissue that contains fat. A changing balance between aqueous and lipid components affects both the proton density and T_1 [81], and this will be a problem even in non-fatty tissue since the disruption of tissue itself may give rise to non-aqueous components. In addition to the observed change being a multicomponent effect, there is a strong dependence on tissue-type as shown in Table 1, a limited linearity range and hysteresis, although reversible T_1 thermal coefficients have also been reported.

Even if the effects of the physiological response of tissue to thermal treatment (protein denaturation, swelling, oedema, and blood degradation) can be modelled, it is unlikely that this would serve any practical purpose, given the complex microenvironment and inhomogeneity of most tumours. These issues render the T_1 method mainly suitable as a qualitative tool in-vivo [3,26], although doubt has been cast over its effectiveness even in this context in a recent study [26]. On the other hand, provided calibration is accurate, the limited linearity of dT_1/dT provides an opportunity to confirm cell death quantitatively [77].

Recently interest has also revived in the use of MR-thermometry for monitoring cryoablations [24,136] and the temperature of adipose tissue [37,55,74,81,137]. When T_1 is used to monitor ablations of fatty tissue such as breast, water must be suppressed [138] or water and fat signals separated [55,77] for improved accuracy. The need to separate the methylene and methyl protons of fatty acids was also highlighted in [81]. When using the temperature coefficient of T_1 of CH_2 only, in tissue with a mixed content, an error of up to 3.3 °C could arise due to the signal containing 18 % CH_3.

The variable flip angle method for T_1 mapping has been shown to produce good results in-vivo using a hybrid T_1/PRF thermometry approach [55,137]. However, simultaneously satisfying the need for fast scanning times and precision in both PRF and T_1 measurements is not trivial. In [55], a multi-echo sequence was used to improve the precision of both PRF and T_1 methods by a factor of 3. Hybrid PRF/T_1 approaches, where T_1 is indirectly measured through the magnitude signal change have also been explored [134].

Methods based on M_0 have been less popular [128], mainly due to the very small thermal coefficient, which implies that a high signal-to-noise ratio (SNR) is required. In addition, long TRs are required to eliminate changes in T_1, making it altogether less suitable for real-time measurements. Although T_2/T_2*- based thermometry has not been popular, it has been recognised for its potential during cryoablations [79,133] to confirm necrosis [3,78] and monitor heating of fatty tissue [74,76,80,81,138] (see Table 2).

Limitations in methods based on the chemical shift of water proton

PRF MR-thermometry is generally the method of choice for organs with sufficient water content, because the temperature range of linearity is a good match to the ablation temperature range. In addition, tissue–type independence mitigates the need for calibrations prior to every treatment. Most commonly, it is used in baseline subtraction mode, where a phase image acquired before heating is subtracted from an image during heating.

Differential measurement makes the method sensitive to all non-temperature related effects that alter the local magnetic field between scans. These include a) drift in the static field [146], b) patient motion [16,63,147], c) local or global changes in magnetic susceptibility (e.g. due to tissue swelling [148], fat [46,161] air [149], movement of interstitial applicators [43] or injection of contrast agent [150]), which can be altered by heating itself [49]. For example, although the screening constant of fat is not temperature-dependent, its susceptibility is, and so is the susceptibility of every other tissue, thus introducing weak tissue-type dependence.

Static magnetic field drifts are mainly problematic in lengthy thermal therapies. To avoid these, standard schemes include subtraction of phase changes in a non-heated region of interest (ROI) [3] or in specific phantoms whose PRF is temperature independent. These can be intrinsic, such as subcutaneous fat/lipids [39,63,98,151] or external, mainly in ex-vivo studies. The intrinsic approach becomes less effective when water and fat components are not homogeneously distributed [41] and when field disturbances are large [96,151].

Fat-referenced phase mapping PRF thermometry offers high spatio-temporal resolution, unlike spectroscopic methods. With spectroscopic PRF, the water protons and the reference moieties in the observation region will in principle be affected by the same susceptibility changes and field drifts at a given time, and therefore these will cancel out. However, large voxels are typically used to obtain sufficient SNR, compromising the spatial resolution and increasing the chances of magnetic field inhomogeneity in the same voxel [96,152].

Intra-voxel temperature gradients will also cause errors due to the temperature-dependence of the susceptibility. High SNR is critical to obtaining accurate results in tissue that contains only a small amount of fat such as liver (where fat is only 3% of water content [151]). Additionally, high SNR could alleviate signal averaging, which will in turn improve the temperature resolution; we will return to this point later.

With phase mapping PRF thermometry, the sensitivity to motion is particularly significant. Motion between scans leads to errors due to misalignment of the images acquired during ablation from the baseline. Similarly, intrascan motion leads to errors due to spatial inhomogeneities and shape-induced body susceptibility changes, for example in, respiration. Although breathing is the main source of motion, the physiological response of tissue to heating can also lead to changes in shape (e.g. swelling, peristalsis, tension).

Breath hold is not possible during thermal treatments lasting several minutes. Tracking navigator echoes and synchronization of the image acquisition to the breathing cycle using respiratory belts can be effective in minimizing errors due to mis-registration [26,50,62,68]. However, these measures cannot help with irregular movement. Multi-baseline approaches are even more effective [16]. A number of baseline images are acquired, forming a library and the baseline image that scores the highest correlation factor with the n^{th} image acquired during ablation is then selected from the library for subtraction [60,69].

Further improvements are offered by reference-less methods [126,153], whereby a background phase is derived from the n^{th} image during ablation. This is achieved by fitting a polynomial to the surrounding unheated region and extrapolating to the heated region, thus avoiding subtraction with a separate image [21,154]. This approach is only successful if sufficient SNR is available, and if water-fat interfaces which can lead to inaccurate polynomial fitting are absent. To avoid the latter, fat can be suppressed or water-selective sequences can be used [16,60,69].

Spectroscopic PRF MR-thermometry is inherently reference-less in the sense that the temperature is not derived relative to an initial temperature at $t = 0$, but instead to an internal reference peak at every time point. In the brain, the proton resonances from a low concentration of brain metabolites (NAA, choline and creatine) are typically used [93,95,118,119,152,155,156]. The methylene lipid resonance in breast [157] or liver and the citrate proton signal in the prostate have also been suggested as internal temperature reference signals [158], although the latter has not been followed up since.

Single-voxel spectroscopy and spectroscopic imaging methods have been employed in-vivo but SNR and scan time become issues [95,157]. As a result, these techniques have not yet proved clinically viable although they perform well in phantom or in-vivo studies [118,134,158]. Accurate calibration in-vivo is also challenging [96,156,157]. High sensitivity is required to detect small internal concentrations of the reference metabolite signals (of the order of 10 mM [95, 158]) and which is still insufficient even when large voxels are used.

Moreover, it is difficult to measure the resonance frequencies of the water and reference peaks accurately enough [99,119,133]. Sufficient attenuation of the water peak is essential to render the measurement possible without saturating the receive electronics [1,95] and this can lead to errors in accurately estimating the resonance of water. It will also inevitably lead to attenuation of the already weak reference signals resulting in poor measurements [99], especially when the SNR is low. Other issues include the impact of pH and protein content [105,159,160] and the inhomogeneity of fat and water content [96,157].

Although fat can be used to correct for effects that are unrelated to temperature, its presence is a significant problem too. Dynamic changes in the fat content during treatment will lead to temperature errors when the phase mapping approach is used. The chemical shift of fat relative to water is 3.5 ppm. Changes of that order due to changes in the fat content are larger than those induced by the small thermal coefficient of -0.01 ppm/°C [46]. Consequently, effects of this nature will mask the changes of phase due to temperature.

Despite the electron screening constant of fat not being temperature dependent, its susceptibility is [161], again introducing temperature errors even when suppression techniques are employed [41]. Fat suppression should be used for accurate results when the tissue mostly contains water [48]. PRF methods cannot be used to measure the temperature of predominantly fatty tissue such the breast, in which case a hybrid thermometry method is more suitable [55,98]. Finally, thermally induced changes in conductivity will also cause the phase shift to scale inaccurately with *TE*, especially when temperature measurements are performed over a large volume and over a long time [162].

Limitations in methods based on the diffusion coefficient

Since Le Bihan [144] first demonstrated diffusion-based MR-thermometry there has been limited investigation of this parameter [163]. Interest has recently revived for assessment of brain temperature [164-167] or diagnosis of multiple sclerosis [117] and some of the proposed schemes based on $D(T)$ are now clinically used. Problems include anisotropy, long acquisition time, sensitivity to motion and tissue-type dependence. Non-temperature related dynamic effects that may alter the molecular diffusion are also an issue, explaining the lack of popularity for thermal therapies as an application area.

General limitations: SNR and spatio-temporal resolution

The standard deviation of temperature (TSD) is proportional to 1/SNR. High SNR is required for accurate real-time MR-thermometry, precise calibration of small MR-thermal coefficients, and quantification and exclusion of non-temperature related effects (which are very hard to detect and interpret otherwise). It enables faster sequences that minimize motion artefacts and provides sufficient resolution to monitor vital structures near the ablation site, permitting procedures that are currently excluded by existing protocols [27].

High spatial and temporal resolution is a problem common to all in-vivo MR-thermometry techniques where averaging is often not an option. Temporal resolution is particularly important in fast moving organs ablated with HIFU sources, which induce rapid heating. Motion introduces artefacts (e.g. blurring and ghosting) that result in deterioration of the image quality independently of the method used for thermometry.

Interstitial micro-coils have received considerable attention from the MRI and spectroscopy communities due to the local SNR gain they offer compared to surface array coils [168]. However, little attention has been paid to their use in MR-thermometry [28,30,169,170]. This can be attributed partly to incompatibility with non-invasive thermal therapies and partly to the lack of cost-effective, scalable and reproducible receivers. Recently a micro-coil receiver with these characteristics was shown to provide an excellent solution to improved MR-thermometry during minimally invasive LITT ablations and its clinical utility was confirmed on studies at 3T on liver-mimicking gel and ex-vivo porcine liver specimens [169].

The receiver consists of a copper-clad Kapton thin film (25 μm Kapton® HN, DuPont High Performance Films), patterned to form a two-turn spiral inductor with a pair of integrated capacitors C_T and C_M for tuning and matching. Figure 5 shows the thermal delivery system (a Somatex Laser Applicator) integrated with an MR-imaging device based on the thin-film micro-coil (OD of the modified applicator is 4.8 mm). Figure 6 shows the arrangement used to assess its performance for PRF MR-thermometry based on phase-mapping, and compare it with that of the cardiac array coil used at St. Mary's Hospital [169].

Figure 5 Somatex laser applicator integrated with a micro-coil for operation at 3T.

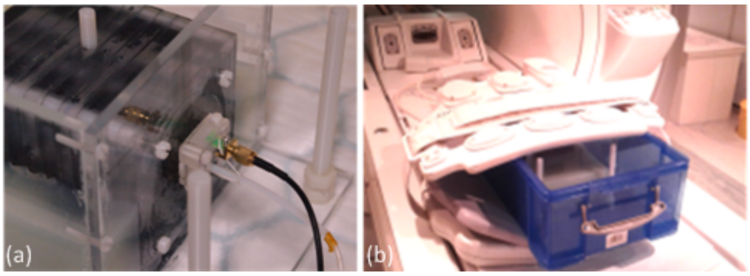

Figure 6 a) Ablation phantom used for phase mapping PRF MR-thermometry studies and b) arrangement for cardiac coil MR-guided LITT in the 3T scanner at St. Mary's Hospital, London.

A Nd:YAG laser (MY 30, Marting Medizin-Technik, Tuttlingen, Germany) with a wavelength of 1064 nm and 25 W output power was used during ablations. The internal circulation cooling system of the applicator was maintained by a continuous flow of 0.9 % NaCl at a rate of 60 ml/min. The laser light was delivered through a 12 m long fibre with a 400 μm diameter core and a 20 mm diffuser active tip (Surgical Laser Technology).

Fibre optic sensors based on fluorescence lifetime (Type 790, Luxtron, Santa Clara, CA, USA), with accuracy ± 0.1 ºC, were used to provide references against the MR-inferred temperatures at d = 5 mm (L_1) and d = 10 mm (L_2) relative to the probe in each monitored slice during the ablation. The two axial slices containing the reference thermometers were monitored (2D GRE thermometry sequence with TR = 7.976 ms, TE = 3.872 ms, FA = 20^o, temporal resolution = 6 s, voxel size = 0.47 mm x 0.47 mm x 10 mm, FOV = 120 mm x 120 mm, pixel BW = 244.141 Hz/pixel).

Figures 7a and 7b show micro-coil axial baseline thermometry images containing the fluoro-optic sensor L_1 at d = 5 mm. Both the micro-coil magnitude and phase images are of good quality, free from artefacts and the fluoro-optic sensor can be clearly seen. Symmetrical patterns of voids near the micro-coil conductors affect the image. Their origin is imperfect decoupling and they occur with all coils and all decoupling schemes, but are generally not noticed because of their short range. Although they can be minimized, they will always be obvious when a local coil is completely immersed in a signal source. The sensitivity is non-uniform and the micro-coil is only able to image a small field-of-view (FOV).

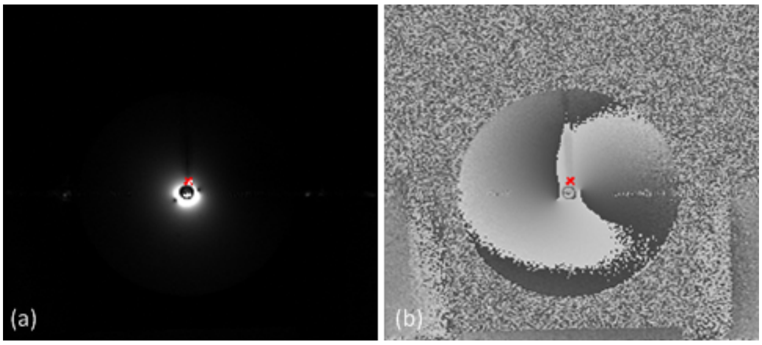

Figure 7 Micro-coil baseline images, showing the sensor L_1: a) magnitude and b) phase.

Figure 8 is a Bald-Altman plot which indicates the degree of correlation with L_1 in each case, in the 2x2 ROI below the thermometer shown in Figure 7b. The advantage of the micro-coil is obvious. The array coil data are significantly noisier. The thermal coefficient a was determined as -0.01 ± 0.009 ppm/ºC from the linear fit of micro-coil phase differences plotted against the temperature differences recorded with L_1. The maximum temperature error is equal to 6 ºC for the micro-coil while the corresponding value for the array coil is 20 ºC.

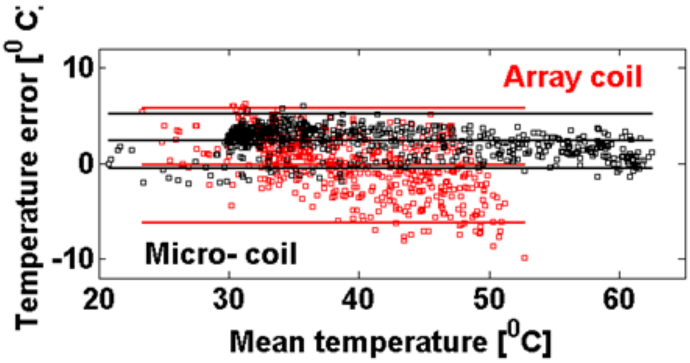

Figure 8 Bald-Altman plots of temperature errors (the difference between the MR-inferred and the fluoro-optic temperatures) derived from the micro-coil and array coil at L_1.

Although non-heated ROIs were used to correct for field drifts, slight deviations from the fluoro-optic temperatures remain. This effect could be attributed to changes in susceptibility or electrical conductivity of the gel with temperature [162]. For example, thermal expansion, or changes in the susceptibility of air bubbles in the ablation phantom might have affected the measurements [100]. The importance of correcting for field drifts is highlighted in Figure 9, which compares micro-coil MR-inferred and fluoro-optic temperatures (without correction for field drifts). Errors clearly become significant at temperatures above 40ºC.

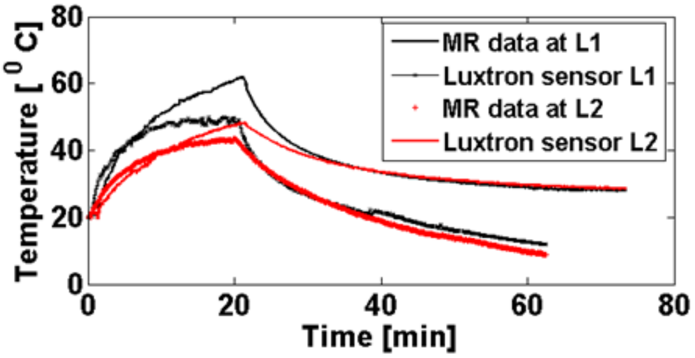

Figure 9 Micro-coil MR-derived temperatures (without correction for field drift) versus fluoro-optic temperature readings.

The choice of the non-heated ROI plays a significant role on how effective the correction becomes. The ROI must be uniform and of good SNR, otherwise noise is introduced into the measurement. The small FOV and non-uniform sensitivity of the micro-coil makes this challenging since the non-heated ROI will normally lie at a distance where the sensitivity is significantly reduced.

Figures 10a and 10b show SNR maps of the two coils. The SNR of the array coil is almost constant, but only equal to only 23. In contrast, the SNR of the micro-coil is locally high but falls off as $1/r^2$. At 5 mm radius, it is 10 times higher and remains 1.5 times higher up to a 15 mm distance. Figure 10c compares the radial variation of the TSD of the two coils. The TSD is a measure of the noise in the temperature measurement and it is inversely proportional to the SNR:

$$TSD = \frac{0.66}{SNR.\alpha.\gamma.TE.B_o} \tag{14}$$

The TSD of the micro-coil remains < 0.75 ºC up to a radius of 20 mm (and < 3 ºC up to 30 mm). Despite its small FOV and non-uniform sensitivity, the micro-coil can provide 10 times less noisy temperature measurements at the margins of small lesions, an impressive result. Even for larger lesions, the TSD will be 1.5 times lower at the margins. The two receivers perform comparably at a radius of 20 mm.

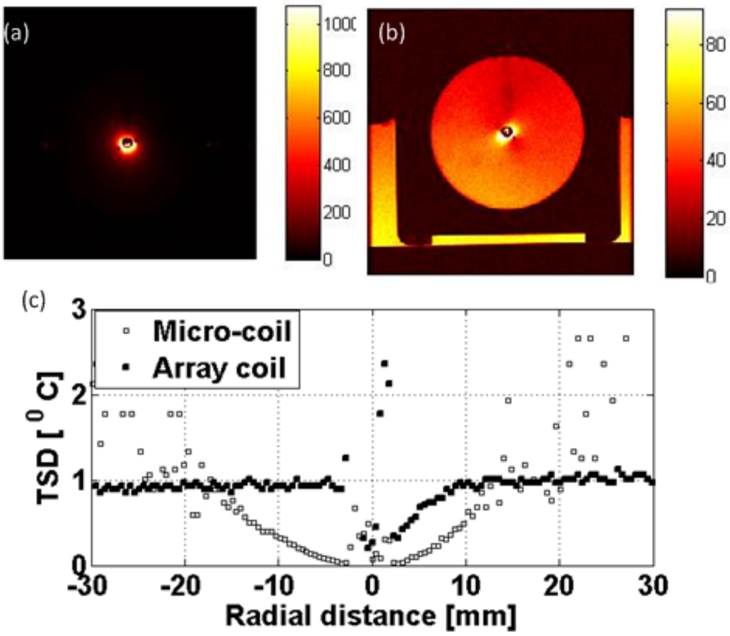

Figure 10 SNR maps of the axial thermometry slice corresponding to L_1: a) micro-coil, b) array coil, c) radial variation of TSD [°C].

Figure 11 compares the maximum temperature error of the two coils during respiratory-gated MR-thermometry of an unheated liver-mimicking phantom, using a motion simulator to simulate movement due to breathing [169]. The data shows the errors due to local susceptibility variations. The micro-coil has a much smaller deviation from the baseline temperature of 20 °C. This result implies that faster sequences can be used with the micro-coil while still achieving a useful SNR.

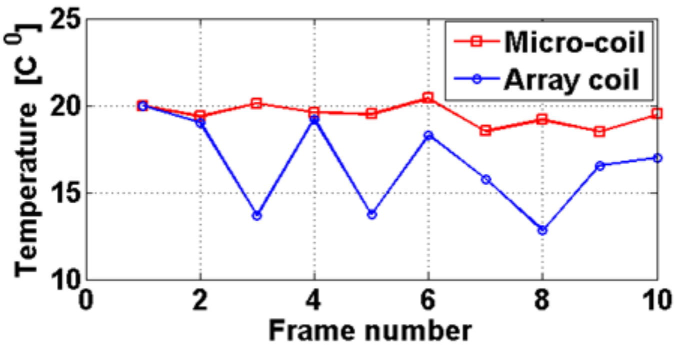

Figure 11 Comparison of the mean temperature error due to motion during respiratory-gated PRF MR-thermometry, obtained using the micro-coil and array coil. The baseline temperature is 20 °C.

The following example is based on a MR-guided LITT of ex-vivo porcine liver containing only a small amount of fat. It confirms that the excellent sensitivity of the micro-coil allows accurate calibration of the thermal coefficients. Water/fat separation was used, with a two-point Dixon sequence inserted into to the gradient-echo thermometry sequence (slice thickness = 5 mm, slice spacing = 2.5 mm, TR = 6.068 ms, TE = 2.1 ms, FOV = 200 mm x 160 mm, pixel BW = 1302.11 Hz/pixel, temporal resolution = 10 s), and temperatures were derived through changes of the signal intensity.

Two 80 mm x 120 mm and 20 mm thick liver slices were placed inside a 700 ml container with the probe horizontally in between. Two fluoro-optic sensors L_1 and L_2 were immersed in the same plane between the liver slices, at 90^0 to the probe and at distances of 5 mm and 10 mm from the probe respectively. Eight axial slices were monitored, two of which contained reference thermometers. The in-phase and out-of-phase images were reconstructed using in-built scanner software (3T GE Signa Excite).

Figures 12a-c show axial micro-coil magnitude baseline thermometry slices: a) in-phase image, b) out-of-phase image and c) fat image. The in-phase and out-of-phase images are very similar confirming the expected small amount of fat present in the liver. Figure 12d is the water-only baseline image indicating the 2x2 ROI next to the reference thermometer L_1 used for calibration. Figure 12e shows the fat content, which was found as a percentage from the ratio between the pixel-by-pixel signal intensity in the in-phase image and the pixel-by-pixel signal intensity in the sum of the in-phase and out-of-phase images.

The white regions correspond to pixels with a small amount of fat, which can only be detected due to the high sensitivity of the micro-coil. Figure 12f, shows the fat content at the 4th minute of the ablation; this shows that more pixels now appear to contain a small amount of fat, which could be an indication of the release of lipid components (phospholipids) as tissue denatures.

Figure 13a shows the calibration curves in the out-of-phase, water and in-phase images. The slopes of the fitted curves represent the thermal coefficients (β) which have values equal to -0.93 %/^{o}C, -1 %/^{o}C and -1.16 %/^{o}C for the out-of-phase, water and in-phase images respectively. The small difference in the values of the thermal coefficients confirms the presence of only a small amount of fat, and indicates that the micro-coil can differentiate between effects occurring in voxels with a small amount of fat present.

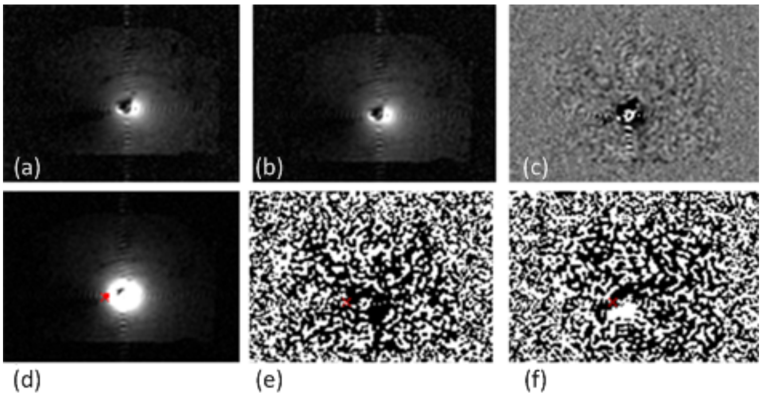

Figure 12 Micro-coil magnitude axial thermometry slices (baseline) corresponding to L_1: a) in-phase image, b) out-of-phase image, c) fat image, d) water image showing the 2x2 pixel ROI next to L_1, e) % fat content image (baseline) and f) % fat content image (at the 4th minute).

The values are very similar to those quoted in other calibration studies [37,97,171]. Deviations from linearity appear at 60 ^{0}C and hysteresis is observed during cooling, as others have observed [77]. Figure 13b shows the normalized calibration curves, from the same ROI for the water and fat images. The normalized difference in signal intensity drops with temperature as -1.2 %/^{o}C in the fat images. The linearity of the fat calibration curve breaks down at approximately 50 ^{o}C, probably due to permanent tissue damage [77].

Figure 14 shows MR-inferred temperatures, based on a) in-phase images with β = -14.2 ^{o}C^{-1}, b) out-of-phase images with β = -11.85 ^{o}C^{-1}. The laser was operated for 4.8 min, causing a rapid temperature rise to 80 ^{o}C. Large deviations from the reference thermometers appear in temperatures derived from the in-phase images compared to those from the out-of-phase images. These observations could indeed indicate some interesting MR-physics as the tissue denatures, which the micro-coil can detect due to its excellent sensitivity.

Figure 15a shows a colour map of the MR-derived temperatures at t = 4 min, based on the out-of-phase images, with β = -11.85 ^{o}C^{-1}. Figure 15b shows a photograph of the corresponding lesion at the end of the ablation, indicating the expected shape and symmetry. Additional opto-thermal characterization of the modified ablation catheter has also been carried out [172], confirming that absorption in the Kapton substrate will not compromise tissue necrosis due to exposure to different temperatures or pose a safety risk due to overheating.

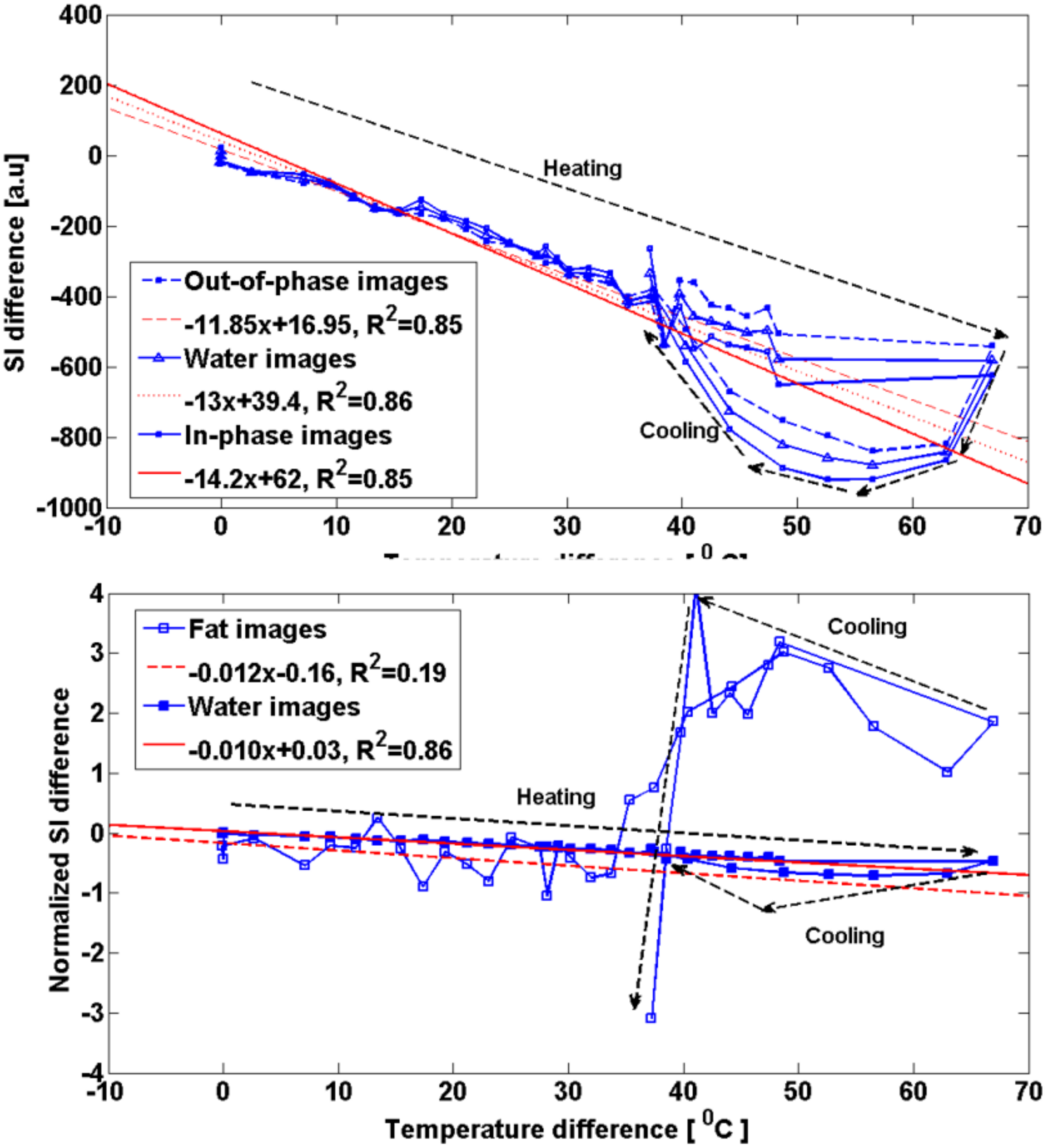

Figure 13 Calibration of the thermal coefficient for micro-coil MR-thermometry based on subtraction of magnitude images: a) out-of-phase, water and in-phase images and b) water and fat images (normalized).

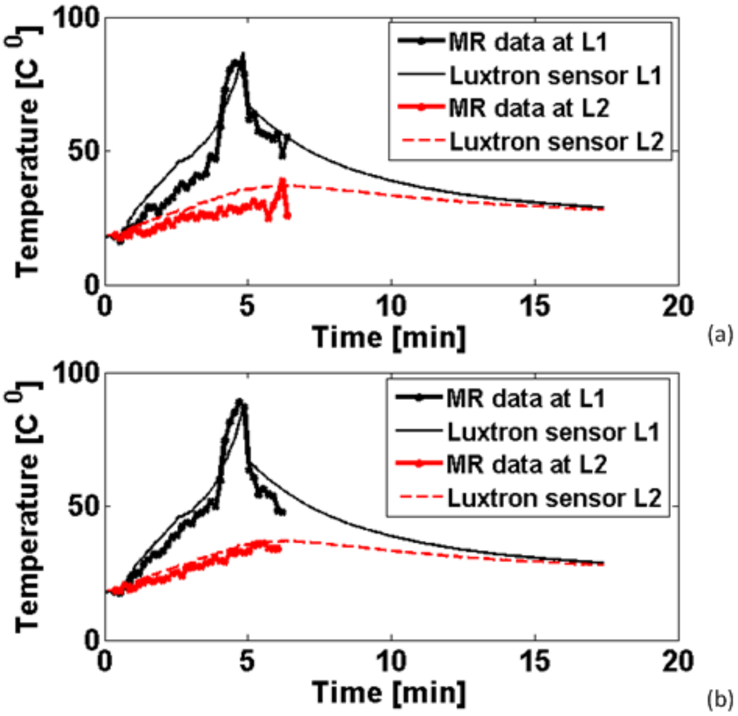

Figure 14 Comparison of temperatures recorded by Luxtron sensors with temperatures derived based on micro-coil MR-thermometry from a) in-phase images with β = -14.2 ºC^{-1}, b) out-of-phase images with β = -11.85 ºC^{-1}.

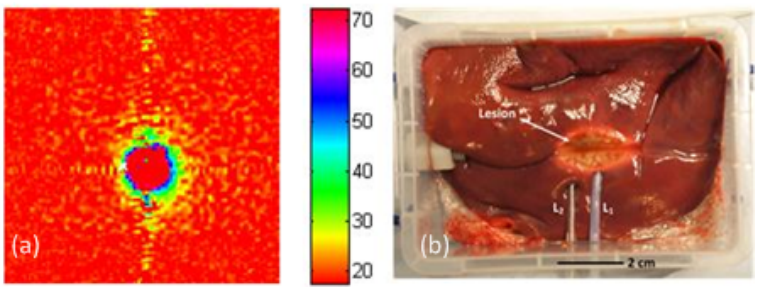

Figure 15 a) Colourmap of the temperature distribution at t = 4 min for the slice containing L_1 based on the out-of-phase images, with β = -11.85 ºC^{-1} and b) photograph of lesion at the end of ablation.

Summary and outlook

MR-thermometry is a mature technique, with confirmed clinical utility despite a set of known residual problems. MR-guided thermal ablations are already or will soon be routinely carried out for the treatment of lesions or other pathologies in the brain, breast, prostate, heart, uterus (for uterine fibroids), liver, and other abdominal organs. To a large extent motion-related errors have been dealt with and preventive or corrective schemes are applied in the clinic. Susceptibility correction algorithms keep emerging and more is understood about the errors caused by fat in tissues (or alternatively how fat can be used to correct for non-temperature related effects).

Significant progress has been made in monitoring tissue that contains fat more accurately by exploiting T_1/T_2 based thermometry, often in combination with PRF-based thermometry. T_1 and T_2 based temperature monitoring during cryoablation or to confirm tissue necrosis also appears promising. However, the proposed techniques have not yet been clinically adopted. Progress has also been made in temperature monitoring of thermal therapies for bone metastases.

Temperature monitoring of the brain has progressively gained clinical acceptance as a diagnostic tool, and spectroscopy- and diffusion-based thermometry have both received attention. In general the possibility of accurate absolute MR-temperature monitoring could prove to be a useful diagnostic tool or a new pathology biomarker. For example, it could help distinguish small variations in temperature due to abnormal tissue metabolism and this possibility is currently being explored.

The potential of spectroscopic approaches to monitor absolute temperature has not yet been fully met, since they are mainly precluded from clinical use due to poor spatio-temporal resolution. A more recent technique [85] based on water saturation shift referencing could be attractive for fatty tissue. It offers high spatio-temporal resolution and provided field inhomogeneities are small it allows for an unbiased assessment of water PRF in the presence of lipid protons, without the need for a priori knowledge of the fat composition and additional data processing steps.

Although the results from this study at high magnetic field strengths (9T and 11 T) are promising, a translation to clinical scanners (1.5T or 3T) may not be as exciting due to lower sensitivity. If this hurdle can be overcome, 3D volumetric temperature mapping with accuracy better than 0.2 °C could be achieved. Another promising approach to absolute thermometry, even in tissue that does not contain temperature-insensitive reference components involves temperature sensitive contrast agents [114]. An important application area is targeted thermally-activated drug delivery which requires accurate temperature monitoring to avoid damage of the surrounding healthy tissue.

A common discussion point is that increased SNR would improve accuracy and spatio-temporal resolution and allow precise calibration. However, researchers use high magnetic field strengths, employ averaging and optimize pulse sequences to increase the SNR. The alternative approach of using internal receivers is being explored by a handful of groups. Disposable internal coils, easily adaptable to existing applicators [169], are suitable for use in minimally invasive thermal therapies and could offer higher SNR, improve calibration accuracy and lead to a better understanding of the impact of biophysical tissue changes on temperature-sensitive MR-parameters.

References

[1] I. R. Young, "Temperature measurement in vivo using NMR", *Encyclopedia of Magnetic Resonance*, Chichester, UK, John Wiley & Sons, Ltd, 2007.

[2] V. Rieke and K. Butts Pauly, "MR thermometry", *J. Magn. Reson. Imaging*, vol. 27, no. 2, pp. 376–390, Feb. 2008.

[3] J. L. Wichmann et al., "Evaluation of MRI T1-based treatment monitoring during laser-induced thermotherapy of liver metastases for necrotic size prediction", *Int. J. Hyperth.*, vol. 30, no. 1, pp. 19-26, Feb. 2014.

[4] M. K. Lam et al., "Quality of MR thermometry during palliative MR-guided high-intensity focused ultrasound (MR-HIFU) treatment of bone metastases", *J. Ther. Ultrasound*, vol. 3, no. 1, pp. 5, Mar. 2015.

[5] J. L. Chin et al., "Magnetic resonance imaging–guided transurethral ultrasound ablation of prostate tissue in patients with localized prostate cancer: A prospective phase 1 clinical trial", *Eur. Urol.*, Jan. 2016, doi: 10.1016/j.eururo.2015.12.029.

[6] N. V. Patel et al., "Does the real-time thermal damage estimate allow for estimation of tumor control after MRI-guided laser-induced thermal therapy? Initial experience with recurrent intracranial ependymomas", *J. Neurosurg. Pediatr.*, vol. 15, no. 4, pp. 363–371, Apr. 2015.

[7] R. Deckers et al., "Performance analysis of a dedicated breast MR-HIFU system for tumor ablation in breast cancer patients", *Phys. Med. Biol.*, vol. 60, no. 14, pp. 5527–42, Jul. 2015.

[8] R. R. Bitton et al., "Improving thermal dose accuracy in magnetic resonance-guided focused ultrasound surgery: Long-term thermometry using a prior baseline as a reference", *J. Magn. Reson. Imaging*, vol. 43, no.1, pp. 181-9, Jun. 2016.

[9] R. Medvid et al., "Current Applications of MRI-Guided Laser Interstitial Thermal Therapy in the Treatment of Brain Neoplasms and Epilepsy: A Radiologic and Neurosurgical Overview", *Am. J. Neuroradiol.*, vol. 36, no. 11, pp. 1998–2006, Nov. 2015.

[10] H. Odéen et al., "Treatment envelope evaluation in transcranial magnetic resonance-guided focused ultrasound utilizing 3D MR thermometry", *J. Ther. Ultrasound*, vol. 2, no. 19, pp. 1-11, Oct. 2014.

[11] D. Coluccia et al., "First noninvasive thermal ablation of a brain tumor with MR-guided focused ultrasound", *J. Ther. Ultrasound*, vol. 2, no. 17, pp. 1-7, Oct. 2014.

[12] T. Dadakova et al., "Fast PRF-based MR thermometry using double-echo EPI: in vivo comparison in a clinical hyperthermia setting", *Magn. Reson. Mater. Physics, Biol. Med.*, vol. 28, no. 4, pp. 305–314, Nov. 2014.

[13] A. Schmitt, C. Mougenot, and R. Chopra, "Spatiotemporal filtering of MR-temperature artifacts arising from bowel motion during transurethral MR-HIFU", *Med. Phys.*, vol. 41, no. 11, pp. 113302, Nov. 2014.

[14] A. M. Mohammadi and J. L. Schroeder, "Laser interstitial thermal therapy in treatment of brain tumors – the NeuroBlate System", *Expert Rev. Med. Devices*, vol. 11, no. 2, pp. 109-19, Feb. 2014.

[15] A. H. Hawasli et al., "Magnetic resonance imaging-guided focused laser interstitial thermal therapy for intracranial lesions: single-institution series", *Neurosurgery*, vol. 73, no. 6, pp. 1007–17, Dec. 2013.

[16] V. Rieke et al., "Comparison of temperature processing methods for monitoring focused ultrasound ablation in the brain", *J. Magn. Reson. Imaging*, vol. 38, no. 6, pp. 1462–1471, Dec. 2013.

[17] A. Carpentier et al., "MR-guided laser-induced thermal therapy (LITT) for recurrent glioblastomas", *Lasers Surg. Med.*, vol. 44, no. 5, pp. 361–368, Jul. 2012.

[18] H. Rempp et al., "Threshold-based prediction of the coagulation zone in sequential temperature mapping in MR-guided radiofrequency ablation of liver tumours", *Eur. Radiol.*, vol. 22, no. 5, pp. 1091–1100, Nov. 2011.

[19] A. Kickhefel et al., "Clinical evaluation of MR temperature monitoring of laser-induced thermotherapy in human liver using the proton-resonance-frequency method and predictive models of cell death", *J. Magn. Reson. Imaging*, vol. 33, no. 3, pp. 704–709, Mar. 2011.

[20] S. Terraz et al., “Radiofrequency ablation of small liver malignancies under magnetic resonance guidance: progress in targeting and preliminary observations with temperature monitoring”, *Eur. Radiol.*, vol. 20, no. 4, pp. 886–97, Apr. 2010.

[21] A. B. Holbrook et al., “Real-time MR thermometry for monitoring HIFU ablations of the liver”, *Magn. Reson. Med.*, vol. 63, no. 2, pp. 365–73, Feb. 2010.

[22] M. Lepetit-Coiffé et al., “Real-time monitoring of radiofrequency ablation of liver tumors using thermal-dose calculation by MR temperature imaging: initial results in nine patients, including follow-up”, *Eur. Radiol.*, vol. 20, no. 1, pp. 193–201, Aug. 2009.

[23] O. I. Craciunescu et al., “Accuracy of real time noninvasive temperature measurements using magnetic resonance thermal imaging in patients treated for high grade extremity soft tissue sarcomas”, *Med. Phys.*, vol. 36, no. 11, pp. 4848, Oct. 2009.

[24] C. G. Overduin et al., “T1-weighted MR image contrast around a cryoablation ice-ball: a phantom study and initial comparison with in vivo findings”, *Med. Phys.*, vol. 41, no. 11, pp. 112301, Nov. 2014.

[25] D. A. Woodrum et al., “Magnetic resonance imaging-guided cryoablation of recurrent prostate cancer after radical prostatectomy: initial single institution experience”, *Urology*, vol. 82, no. 4, pp. 870–5, Oct. 2013.

[26] C. Rosenberg et al., “PRFS-based MR thermometry versus an alternative T1 magnitude method-comparative performance predicting thermally induced necrosis in hepatic tumor ablation”, *PLoS One*, vol. 8, no. 10, pp. e78559, Jan. 2013.

[27] G. Bruggmoser et al., “Guideline for the clinical application, documentation and analysis of clinical studies for regional deep hyperthermia: quality management in regional deep hyperthermia”, *Strahlenther. Onkol.*, vol. 188 Suppl, pp. 198–211, Sep. 2012.

[28] N. A. Volland et al., “Initial feasibility testing of limited field of view magnetic resonance thermometry using a local cardiac radiofrequency coil”, *Magn. Reson. Med.*, vol. 70, no. 4, pp. 994–1004, Oct. 2013.

[29] E. C. Mbalisike et al., “Image-guided microwave thermoablation of hepatic tumours using novel robotic guidance: an early experience”, *Eur. Radiol.*, vol. 25, no. 2, pp. 454–62, Feb. 2015.

[30] M. Rata et al., “Endoluminal MR-guided ultrasonic applicator embedding cylindrical phased-array transducers and opposed-solenoid detection coil”, *Magn. Reson. Med.*,

vol. 73, no. 1, pp. 417–426, Jan. 2014.

[31] F. Streitparth et al., “Laser-induced thermotherapy (LITT)--evaluation of a miniaturised applicator and implementation in a 1.0-T high-field open MRI applying a porcine liver model”, *Eur. Radiol.*, vol. 20, no. 11, pp. 2671–8, Nov. 2010.

[32] W. C. M. Numan et al., “Exploration of MR-guided head and neck hyperthermia by phantom testing of a modified prototype applicator for use with proton resonance frequency shift thermometry”, *Int. J. Hyperth.*, vol. 30, no. 3, pp. 184-91, May. 2014.

[33] F. Zucconi et al., “Analysis and reduction of thermal dose errors in MRgFUS treatment”, *Phys. Medica*, vol. 30, no. 1, pp. 111–116, Feb. 2014.

[34] C. P. Favazza et al., “An investigation of the effects from a urethral warming system on temperature distributions during cryoablation treatment of the prostate: A phantom study”, *Cryobiology*, vol. 69, no. 1, pp. 128–133, Aug. 2014.

[35] B. T. Svedin, A. Payne, and D. L. Parker, “Respiration artifact correction in three-dimensional proton resonance frequency MR thermometry using phase navigators”, *Magn. Reson. Med.*, Aug. 2015., doi: 10.1002/mrm.25860

[36] S. Vallo et al., “MR-guided laser-induced thermotherapy in ex vivo porcine kidney: Comparison of four different imaging sequences”, *Lasers Surg. Med.*, vol. 46, no. 7, pp. 558–562, Sep. 2014.

[37] M. Diakite et al., “Toward real-time temperature monitoring in fat and aqueous tissue during magnetic resonance-guided high-intensity focused ultrasound using a three-dimensional proton resonance frequency T1 method”, *Magn. Reson. Med.*, vol. 72, no. 1, pp. 178–187, Jul. 2014.

[38] L. W. Hofstetter et al., “Fat-referenced MR thermometry in the breast and prostate using IDEAL”, *J. Magn. Reson. Imaging*, vol. 36, no. 3, pp. 722–32, Sep. 2012.

[39] B. A. Taylor et al., “Measurement of temperature dependent changes in bone marrow using a rapid chemical shift imaging technique”, *J. Magn. Reson. Imaging*, vol. 33, no. 5, pp. 1128–35, May 2011.

[40] C. S. Mei et al., “Combining two-dimensional spatially selective RF excitation, parallel imaging, and UNFOLD for accelerated MR thermometry imaging”, *Magn. Reson. Med.*, vol. 66, pp. 112–122, Jul. 2011.

[41] S. M. Sprinkhuizen et al., “Temperature-induced tissue susceptibility changes lead to significant temperature errors in PRFS-based MR thermometry during thermal interventions”, *Magn. Reson. Med.*, vol. 64, no. 5, pp. 1360–72, Nov. 2010.

[42] A. Kickhefel et al., “Accuracy of real-time MR temperature mapping in the brain: a comparison of fast sequences”, *Phys. Med.*, vol. 26, no. 4, pp. 192–201, Oct. 2010.

[43] X. Zhou et al., “Temperature measurement error reduction for MRI-guided HIFU treatment”, *Int. J. Hyperth.*, vol. 26, no. 4, pp. 347-58, May 2010.

[44] U. Wonneberger et al., “Evaluation of thermometric monitoring for intradiscal laser ablation in an open 1.0 T MR scanner”, *Int. J. Hyperth.*, vol. 26, no. 4, pp. 295-304, May 2010.

[45] X. Pan et al., “Model-based PRFS thermometry using fat as the internal reference and the extended Prony algorithm for model fitting”, *Magn. Reson. Imaging*, vol. 28, no. 3, pp. 418–26, Apr. 2010.

[46] D. C. Karampinos et al., “Chemical shift-based water/fat separation in the presence of susceptibility-induced fat resonance shift”, *Magn. Reson. Med.*, vol. 68, no. 5, pp. 1495–505, Nov. 2012.

[47] C. Wyatt et al., “Comprehensive analysis of the Cramer-Rao bounds for magnetic resonance temperature change measurement in fat-water voxels using multi-echo imaging”, *MAGMA*, vol. 25, no. 1, pp. 49–61, Feb. 2012.

[48] J. Yuan et al., “Fast fat-suppressed reduced field-of-view temperature mapping using 2DRF excitation pulses”, *J. Magn. Reson.*, vol. 210, no. 1, pp. 38–43, May 2011.

[49] S. Sprinkhuizen et al., “Heating of fat leads to significant temperature errors in PRFS based MR thermometry”, in *Proceedings 17th Scientific Meeting, International Society for Magnetic Resonance in Medicine*, Honolulu, p. 2532, 2009

[50] N. Boulant et al., “FID navigator-based MR thermometry method to monitor small temperature changes in the brain of ventilated animals”, *NMR Biomed.*, vol. 28, no. 1, pp. 101–7, Jan. 2015.

[51] M. Marx and K. Butts Pauly, “Improved MRI thermometry with multiple-echo spirals”, *Magn. Reson. Med.*, Aug. 2015., doi: 10.1002/mrm.25914

[52] P. Gaur et al., “Correcting heat-induced chemical shift distortions in proton resonance frequency-shift thermometry”, *Magn. Reson. Med.*, Aug. 2015, doi: 10.1002/mrm.25899.

[53] S. Dehkharghani et al., “Proton resonance frequency chemical shift thermometry: experimental design and validation toward high-resolution noninvasive temperature monitoring and in vivo experience in a nonhuman primate model of acute ischemic stroke”, *Am. J. Neuroradiol.*, vol. 36, no. 6, pp. 1128–35, Jun. 2015.

[54] M. N. Streicher et al., “Fast accurate MR thermometry using phase referenced asymmetric spin-echo EPI at high field”, *Magn. Reson. Med.*, vol. 71, no. 2, pp. 524–533, Feb. 2014.

[55] N. Todd et al., “In vivo evaluation of multi-echo hybrid PRF/T1 approach for temperature monitoring during breast MR-guided focused ultrasound surgery treatments”, *Magn. Reson. Med.*, vol. 72, no. 3, pp. 793–9, Sep. 2014.

[56] M. Marx et al., “Toward volumetric MR thermometry with the MASTER Sequence”, *IEEE Trans. Med. Imaging*, vol. 34, no. 1, pp. 148–155, Jan. 2014.

[57] B. Z. Fite et al., “Magnetic resonance thermometry at 7T for real-time monitoring and correction of ultrasound induced mild hyperthermia”, *PLoS One*, vol.7, no. 4, e35509 Jan. 2012.

[58] C.-S. S. Mei et al., “Ultrafast 1D MR thermometry using phase or frequency mapping”, *Magn. Reson. Mater. Physics, Biol. Med.*, vol. 25, no. 1, pp. 5–14, Feb. 2012.

[59] B. E. O’Neill et al., “Estimation of thermal dose from MR thermometry during application of nonablative pulsed high intensity focused ultrasound”, *J. Magn. Reson. Imaging*, vol. 35, no. 5, pp. 1169–78, May 2012.

[60] W. A. Grissom et al., “Hybrid referenceless and multibaseline subtraction MR thermometry for monitoring thermal therapies in moving organs”, *Med. Phys.*, vol. 37, no. 9, pp. 5014–5026, Aug. 2010.

[61] R. J. Stafford et al., “Magnetic resonance guided, focal laser induced interstitial thermal therapy in a canine prostate model”, *J. Urol.*, vol. 184, no. 4, pp. 1514–1520, Oct. 2010.

[62] M. Ries et al., “Real-time 3D target tracking in MRI guided focused ultrasound ablations in moving tissues”, *Magn. Reson. Med.*, vol. 64, no. 6, pp. 1704–12, Dec. 2010.

[63] C. R. Wyatt, B. J. Soher, and J. R. MacFall, “Correction of breathing-induced errors in magnetic resonance thermometry of hyperthermia using multiecho field fitting techniques”, *Med. Phys.*, vol. 37, no. 12, pp. 6300–9, Dec. 2010.

[64] E. Delabrousse et al., “Automatic temperature control for MR-guided interstitial ultrasound ablation in liver using a percutaneous applicator: ex vivo and in vivo initial studies”, *Magn. Reson. Med.*, vol. 63, no. 3, pp. 667–79, Mar. 2010.

[65] S. Roujol et al., “Real-time MR-thermometry and dosimetry for interventional

guidance on abdominal organs", *Magn. Reson. Med.*, vol. 63, no. 4, pp. 1080–1087, 2010.

[66] A. Muller et al., "Management of respiratory motion in extracorporeal high-intensity focused ultrasound treatment in upper abdominal organs: current status and perspectives", *Cardiovasc. Intervent. Radiol.*, vol. 36, no. 6, pp. 1464–76, Dec. 2013.

[67] V. Auboiroux et al., "Ultrasonography-based 2D motion-compensated HIFU sonication integrated with reference-free MR temperature monitoring: a feasibility study ex vivo", *Phys. Med. Biol.*, vol. 57, no. 10, pp. N159–N171, May 2012.

[68] F. Maier et al., "Velocity navigator for motion compensated thermometry", *Magn. Reson. Mater. Physics, Biol. Med.*, vol. 25, no. 1, pp. 15–22, Mar. 2011.

[69] B. D. de Senneville et al., "Motion correction in MR thermometry of abdominal organs: A comparison of the referenceless vs. the multibaseline approach", *Magn. Reson. Med.*, vol. 64, no. 5, pp. 1373–1381, Nov. 2010.

[70] M. Han et al., "Quantifying temperature-dependent T1 changes in cortical bone using ultrashort echo-time MRI", *Magn. Reson. Med.*, vol. 74, no. 6, pp. 1548-55, Sep. 2015.

[71] C. Birkl et al., "Temperature-induced changes of magnetic resonance relaxation times in the human brain: a postmortem study", *Magn. Reson. Med.*, vol. 71, no. 4, pp. 1575–80, Apr. 2014.

[72] A. Gangi et al., "Percutaneous MR-guided cryoablation of prostate cancer: initial experience", *Eur. Radiol.*, vol. 22, no. 8, pp. 1829–35, Aug. 2012.

[73] A. Lu et al., "MRI of frozen tissue demonstrates a phase shift", *Magn. Reson. Med.*, vol. 66, no. 6, pp. 1582–9, Dec. 2011.

[74] P. Baron et al., "T1 and T2 temperature dependence of female human breast adipose tissue at 1.5 T: groundwork for monitoring thermal therapies in the breast", *NMR Biomed.*, vol. 28, no. 11, pp.1463-70, Sep. 2015.

[75] G. Allegretti et al., "Magnetic resonance-based thermometry during laser ablation on ex-vivo swine pancreas and liver", *Med. Eng. Phys.*, vol. 37, no. 7, pp. 631–41, Jul. 2015.

[76] M. Parmala et al., "Temperature measurement in human fat with T2 imaging", *J. Magn. Reson. Imaging*, Oct. 2015., doi: 10.1002/jmri.25064.

[77] M. Diakite et al., "Irreversible change in the T1 temperature dependence with thermal dose using the proton resonance frequency-T1 technique", *Magn. Reson. Med.*, vol. 69, no. 4, pp. 1122–30, Apr. 2013.

[78] B. A. Taylor et al., “Correlation between the temperature dependence of intrinsic MR parameters and thermal dose measured by a rapid chemical shift imaging technique”, *NMR Biomed.*, vol. 24, no. 10, pp. 1414–1421, Dec. 2011.

[79] E. A. Kaye et al., “Consistency of signal intensity and T2* in frozen ex vivo heart muscle, kidney, and liver tissue”, *J. Magn. Reson. Imaging*, vol. 31, no. 3, pp. 719–724, Mar. 2010.

[80] P. M. Winter et al., “Initial investigation of a novel noninvasive weight loss therapy using MRI-Guided high intensity focused ultrasound (MR-HIFU) of visceral fat”, *Magn. Reson. Med.*, Aug. 2015., doi: 10.1002/mrm.25883.

[81] K. Kuroda et al., “Temperature Dependence of Relaxation Times in Proton Components of Fatty Acids”, *Magn. Reson. Med. Sci.*, vol. 10, no. 3, pp. 177–183, Sep. 2011.

[82] S. J. C. G. Hectors et al., “T1 ϱ mapping for the evaluation of high intensity focused ultrasound tumor treatment”, *Magn. Reson. Med.*, vol. 73, no. 4, pp. 1593–601, Apr. 2015.

[83] T. J. Vogl et al., “MR-based Thermometry of Laser Induced Thermotherapy: Temperature Accuracy and Temporal Resolution In vitro at 0.2 and 1.5 T Magnetic Field Strengths”, *Lasers Surg. Med.*, vol. 44, no. 3, pp. 257–265, Mar. 2012.

[84] S. M. Sprinkhuizen et al., “Absolute MR thermometry using time-domain analysis of multi-gradient-echo magnitude images”, *Magn. Reson. Med.*, vol. 64, no. 1, pp. 239–248, Jul. 2010.

[85] G. Liu et al., “Non-invasive temperature mapping using temperature-responsive water saturation shift referencing (T-WASSR) MRI”, *NMR Biomed.*, vol. 27, no. 3, pp. 320–31, Mar. 2014.

[86] R. M. Davis and W. S. Warren, “Intermolecular zero quantum coherences enable accurate temperature imaging in red bone marrow”, *Magn. Reson. Med.*, vol. 74, pp. 63–70, Jul. 2014.

[87] P. Gaur and W. A. Grissom, “Accelerated MRI thermometry by direct estimation of temperature from undersampled k-space data”, *Magn. Reson. Med.*, vol. 73, no. 5, pp. 1914–25, May 2015.

[88] Z. Cao et al., “Complex difference constrained compressed sensing reconstruction for accelerated PRF thermometry with application to MRI-induced RF heating”, *Magn. Reson. Med.*, vol. 73, no. 4, pp. 1420–31, Apr. 2015.

[89] N. Todd et al., “Toward real-time availability of 3D temperature maps created with temporally constrained reconstruction”, *Magn. Reson. Med.*, vol. 71, no. 4, pp. 1394–404, Apr. 2014.

[90] P. Wang and O. Unal, “Motion-compensated real-time MR thermometry augmented by tracking coils”, *J. Magn. Reson. Imaging*, vol. 41, no. 3, pp. 851–857, Mar. 2014.

[91] T. Inoue et al., “Noninvasive measurement of human brain temperature adjacent to arteriovenous malformation using 3.0 T magnetic resonance spectroscopy”, *Clin. Neurol. Neurosurg.*, vol. 115, no. 4, pp. 445–9, Apr. 2013.

[92] J. Weis et al., “Phase-difference and spectroscopic imaging for monitoring of human brain temperature during cooling”, *Magn. Reson. Imaging*, vol. 30, no. 10, pp. 1505–11, Dec. 2012.

[93] E. B. Cady, J. Penrice, and N. J. Robertson, “Improved reproducibility of MRS regional brain thermometry by ‘amplitude-weighted combination”, *NMR Biomed.*, vol. 24, no. 7, pp. 865–72, Aug. 2011.

[94] L. Covaciu et al., “Human brain MR spectroscopy thermometry using metabolite aqueous-solution calibrations”, *J. Magn. Reson. Imaging*, vol. 31, no. 4, pp. 807–14, Apr. 2010.

[95] K. Kuroda, “Non-invasive MR thermography using the water proton chemical shift”, *Int. J. Hyperth.*, vol.21, no.6, pp.547-60, Jul. 2009.

[96] P. Baron et al., “Influence of water and fat heterogeneity on fat-referenced MR thermometry”, *Magn. Reson. Med.*, May 2015., doi: 10.1002/mrm.25727

[97] B. Bazrafshan et al., “Temperature imaging of laser-induced thermotherapy (LITT) by MRI: evaluation of different sequences in phantom”, *Lasers Med. Sci.*, vol. 29, no. 1, pp. 173–83, Jan. 2014.

[98] P. Baron et al., “Correction of proton resonance frequency shift MR-thermometry errors caused by heat-induced magnetic susceptibility changes during high intensity focused ultrasound ablations in tissues containing fat”, *Magn. Reson. Med.*, vol. 72, no. 6, pp. 1580–1589, Dec. 2014.

[99] H. Odéen et al., “Sampling strategies for subsampled segmented EPI PRF thermometry in MR guided high intensity focused ultrasound”, *Med. Phys.*, vol. 41, no. 9, pp. 092301, Sep. 2014.

[100] M. N. Streicher et al., “Effects of air susceptibility on proton resonance frequency MR thermometry”, *MAGMA*, vol. 25, no. 1, pp. 41–7, Feb. 2012.

[101] A. Kickhefel et al., “Correction of susceptibility-induced GRE phase shift for accurate PRFS thermometry proximal to cryoablation iceball”, *Magn. Reson. Mater. Physics, Biol. Med.*, vol. 25, no. 1, pp. 23–31, Sep. 2011.

[102] B. Madore et al., “Multipathway sequences for MR thermometry”, *Magn. Reson. Med.*, vol. 66, no. 3, pp. 658–68, Sep. 2011.

[103] J. Langley et al., “A self-reference PRF-shift MR thermometry method utilizing the phase gradient”, *Phys. Med. Biol.*, vol. 56, no. 24, pp. N307–20, Dec. 2011.

[104] B. J. Soher et al., “Noninvasive temperature mapping with MRI using chemical shift water-fat separation”, *Magn. Reson. Med.*, vol. 63, no. 5, pp. 1238–1246, May 2010.

[105] J. Luo et al., “Protein-induced water 1H MR frequency shifts: contributions from magnetic susceptibility and exchange effects”, *J. Magn. Reson.*, vol. 202, no. 1, pp. 102–8, Jan. 2010.

[106] C. Li et al., “An internal reference model-based PRF temperature mapping method with Cramer-Rao lower bound noise performance analysis”, *Magn. Reson. Med.*, vol. 62, no. 5, pp. 1251–60, Nov. 2009.

[107] E. Ramsay et al., “MR thermometry in the human prostate gland at 3.0T for transurethral ultrasound therapy”, *J. Magn. Reson. Imaging*, vol. 38, no. 6, pp. 1564–1571, Dec. 2013.

[108] A. Carpentier et al., “Laser thermal therapy: real-time MRI-guided and computer-controlled procedures for metastatic brain tumors”, *Lasers Surg. Med.*, vol. 43, no. 10, pp. 943–50, Dec. 2011.

[109] H. Rempp et al., “Prediction of cell necrosis with sequential temperature mapping after radiofrequency ablation”, *J. Magn. Reson. Imaging*, vol. 30, no. 3, pp. 631–639, Sep. 2009.

[110] D. A. Kunkle and R. G. Uzzo, “Cryoablation or radiofrequency ablation of the small renal mass: a meta-analysis”, *Cancer*, vol. 113, no. 10, pp. 2671–80, Nov. 2008.

[111] M. J. Voogt et al., “Volumetric feedback ablation of uterine fibroids using magnetic resonance-guided high intensity focused ultrasound therapy”, *Eur. Radiol.*, vol. 22, no. 2, pp. 411–7, Feb. 2012.

[112] N. Hijnen, S. Langereis, and H. Grüll, “Magnetic resonance guided high-intensity focused ultrasound for image-guided temperature-induced drug delivery”, *Adv. Drug Deliv. Rev.*, vol. 72, pp. 65–81, Jun. 2014.

[113] C. Lorenzato et al., “Rapid dynamic R1 /R2 */temperature assessment: a method with

potential for monitoring drug delivery", *NMR Biomed.*, vol. 27, no. 11, pp. 1267–74, Nov. 2014.

[114] R. Deckers et al., "Absolute MR thermometry using nanocarriers", *Contrast Media Mol. Imaging*, vol. 9, no. 4, pp. 283–90, Jan. 2014.

[115] U. Reiter et al., "Four-dimensional temperature distributions in red blood cells withdrawn from storage and exposed to ambient temperature: a magnetic resonance thermometry study", *Transfusion*, vol. 53, no. 1, pp. 167–73, Jan. 2013.

[116] C. Birkl et al., "Iron mapping using the temperature dependency of the magnetic susceptibility", *Magn. Reson. Med.*, vol. 73, no. 3, pp. 1282–1288, Mar. 2015.

[117] A. Sai et al., "Diffusion-weighted imaging thermometry in multiple sclerosis", *J. Magn. Reson. Imaging*, vol. 40, no. 3, pp. 649–54, Sep. 2014.

[118] M. J. Thrippleton et al., "Reliability of MRSI brain temperature mapping at 1.5 and 3 T", *NMR Biomed.*, vol. 27, no. 2, pp. 183–90, Feb. 2014.

[119] A. Bainbridge et al., "Regional neonatal brain absolute thermometry by 1H MRS", *NMR Biomed.*, vol. 26, no. 4, pp. 416–23, Apr. 2013.

[120] D. Haddad et al., "Specific identification of iron oxide-labeled stem cells using magnetic field hyperthermia and MR thermometry", *NMR Biomed*, vol. 25, no. 3, pp. 402–409, Mar. 2012.

[121] E. A. Dick and W.M.W. Gedroyc, "ExAblate® magnetic resonance-guided focused ultrasound system in multiple body applications", *Expert Rev. Med. Devices*, vol. 7, no.5, pp. 589-597, May 2010.

[122] V. A. Salgaonkar et al., "Model-based feasibility assessment and evaluation of prostate hyperthermia with a commercial MR-guided endorectal HIFU ablation array", *Med. Phys.*, vol. 41, no. 3, pp. 033301, Mar. 2014.

[123] Z. Tovar-Spinoza et al., "The use of MRI-guided laser-induced thermal ablation for epilepsy", *Childs Nerv. Syst.*, vol. 29, no. 11, pp. 2089–94, Nov. 2013.

[124] E. B. Cady et al., "The estimation of local brain temperature by in vivo 1H magnetic resonance spectroscopy", *Magn. Reson. Med.*, vol. 33, no. 6, pp. 862–867, 1995.

[125] R. J. Corbett eet al., "Validation of a noninvasive method to measure brain temperature in vivo using 1H NMR spectroscopy", *J. Neurochem.*, vol. 64, no. 3, pp. 1224–30, Mar. 1995.

[126] V. Rieke et al., "Referenceless MR thermometry for monitoring thermal ablation in the prostate", *IEEE Trans. Med. Imaging*, vol. 26, no. 6, pp. 813–21, Jun. 2007.

[127] L. Winter et al., “Magnetic resonance thermometry: Methodology, pitfalls and practical solutions”, *Int. J. Hyperthermia*, pp. 1–13, Dec. 2015., doi: 10.3109/02656736.2015.1108462.

[128] J. Chen, B. L. Daniel, and K. B. Pauly, “Investigation of proton density for measuring tissue temperature”, *J. Magn. Reson. Imaging*, vol. 23, no. 3, pp. 430–4, Mar. 2006.

[129] N. Bloembergen, E. Purcell, and R. Pound, “Relaxation Effects in Nuclear Magnetic Resonance Absorption”, *Phys. Rev.*, vol. 73, no. 7, pp. 679–712, Apr. 1948.

[130] I. R. Young et al., “Further observations on the measurement of tissue T1 to monitor temperature in vivo by MRI”, *Magn. Reson. Med.*, vol. 31, no. 3, pp. 342–345, Mar. 1994.

[131] J. P. Wansapura et al., “In vivo MR thermometry of frozen tissue using R2* and signal intensity”, *Acad. Radiol.*, vol. 12, no. 9, pp. 1080–4, Sep. 2005.

[132] K. Butts et al., “Temperature quantitation and mapping of frozen tissue”, *J. Magn. Reson. Imaging*, vol. 13, no. 1, pp. 99–104, Jan. 2001.

[133] A. Lu et al., “Improved slice selection for R2* mapping during cryoablation with eddy current compensation”, *J. Magn. Reson. Imaging*, vol. 28, no. 1, pp. 190–198, Jul. 2008.

[134] E. Ramsay et al.,“Temperature-dependent MR signals in cortical bone: potential for monitoring temperature changes during high-intensity focused ultrasound treatment in bone”, *Magn. Reson. Med.*, vol. 74, no. 4, pp. 1095-102, Oct. 2014.

[135] H. E. Cline et al., “MR temperature mapping of focused ultrasound surgery”, *Magn. Reson. Med.*, vol. 31, no. 6, pp. 628–636, Jun. 1994.

[136] R. Matsumoto, K. Oshio, and F. A. Jolesz, “Monitoring of laser and freezing-induced ablation in the liver with T1-weighted MR imaging”, *J. Magn. Reson. Imaging*, vol. 2, no. 5, pp. 555–562, Sep. 1992.

[137] S. Hey et al., “Simultaneous T1 measurements and proton resonance frequency shift based thermometry using variable flip angles”, *Magn. Reson. Med.*, vol. 67, no. 2, pp. 457–63, Feb. 2012.

[138] P. Baron et al., “In vivo T2 -based MR thermometry in adipose tissue layers for high-intensity focused ultrasound near-field monitoring”, *Magn. Reson. Med.*, vol. 72, no. 4, pp. 1057–1064, Oct. 2014.

[139] E. Ozhinsky et al., “Relationship between temperature and T2 in subcutaneous fat and bone marrow at 3T”, *J. Ther. Ultrasound*, vol. 3, no. Suppl 1, pp. P89, Jun. 2015.

[140] R. D. T. D. Peters, R. S. Hinks, and R. M. Henkelman, "Ex vivo tissue-type independence in proton-resonance frequency shift MR thermometry", *Magn. Reson. Med.*, vol. 40, no. 3, pp. 454–459, Sep. 1998.

[141] J. C. Hindman, "Proton resonance shift of water in the gas and liquid states", *J. Chem. Phys.*, vol. 44, no. 12, pp. 4582, May 1966.

[142] N. McDannold, "Quantitative MRI-based temperature mapping based on the proton resonant frequency shift: Review of validation studies", *Int. J. Hyperth.*, vol. 21, no. 6, pp. 533-46, Jul. 2009.

[143] Y. Ishihara et al., "A precise and fast temperature mapping using water proton chemical shift", *Magn. Reson. Med.*, vol. 34, no. 6, pp. 814–23, Dec. 1995.

[144] D. Le Bihan, J. Delannoy, and R. L. Levin, "Temperature mapping with MR imaging of molecular diffusion: application to hyperthermia", *Radiology*, vol. 171, no. 3, pp. 853–7, Jun. 1989.

[145] I. R. Young et al., "Modeling and observation of temperature changes in vivo using MRI", *Magn. Reson. Med.*, vol. 32, no. 3, pp. 358–69, Sep. 1994.

[146] C.-S. S. Mei et al., "Accurate field mapping in the presence of B_0 inhomogeneities, applied to MR thermometry," *Magn. Reson. Med.*, vol. 73, no. 6, pp. 2142–51, Jun. 2014.

[147] B. D. de Senneville, B. Quesson, and C. T. W. Moonen, "Magnetic resonance temperature imaging", *Int. J. Hyperth.*, vol. 21, no. 6, pp. 515-31, Jul. 2009.

[148] I. R. Young et al., "An evaluation of the effects of susceptibility changes on the water chemical shift method of temperature measurement in human peripheral muscle", *Magn. Reson. Med.*, vol. 36, no. 3, pp. 366–374, Sep. 1996.

[149] M. N. Streicher et al., "Effects of air susceptibility on proton resonance frequency MR thermometry", *MAGMA*, vol. 25, no. 1, pp. 41–7, Feb. 2012.

[150] N. M. Hijnen et al., "The magnetic susceptibility effect of gadolinium-based contrast agents on PRFS-based MR thermometry during thermal interventions", *J. Ther. ultrasound*, vol. 1, no. 1, pp. 1-8, Jan. 2013.

[151] A. V Shmatukha, P. R. Harvey, and C. J. G. Bakker, "Correction of proton resonance frequency shift temperature maps for magnetic field disturbances using fat signal", *J. Magn. Reson. Imaging*, vol. 25, no. 3, pp. 579–87, Mar. 2007.

[152] K. Kuroda et al., "Feasibility of internally referenced brain temperature imaging with a metabolite signal", *Magn. Reson. Med. Sci.*, vol. 2, no. 1, pp. 17–22, Apr. 2003.

[153] R. Salomir et al., "Reference-free PRFS MR-thermometry using near-harmonic 2-D reconstruction of the background phase", *IEEE Trans. Med. Imaging*, vol. 31, no. 2, pp. 287–301, Feb. 2012.

[154] C. Zou et al., "A fast referenceless PRFS-basedMR thermometry by phase finite difference", *Phys. Med. Biol.*, vol. 58, no. 16, pp. 5735–51, Aug. 2013.

[155] J. Weis et al., "Noninvasive monitoring of brain temperature during mild hypothermia", *Magn. Reson. Imaging*, vol. 27, no. 7, pp. 923–32, Sep. 2009.

[156] M. Zhu et al., "Improved calibration technique for in vivo proton MRS thermometry for brain temperature measurement", *Magn. Reson. Med.*, vol. 60, no. 3, pp. 536–541, Sep. 2008.

[157] M. Viallon et al., "Observation and correction of transient cavitation-induced PRFS thermometry artifacts during radiofrequency ablation, using simultaneous Ultrasound/MR imaging", *Med. Phys.*, vol. 37, no. 4, pp. 1491, Mar. 2010.

[158] K. Kuroda, "Internally-referenced measurement of prostate temperature using metabolite signals", *Proc. 8th Scientific Meeting, International Society for Magnetic Resonance in Medicine,* Denver, p. 49, 2000.

[159] B. Babourina-Brooks et al., "MRS thermometry calibration at 3 T: effects of protein, ionic concentration and magnetic field strength", *NMR Biomed.*, vol. 28, no. 7, pp. 792–800, Jul. 2015.

[160] B. Babourina-Brooks et al., "MRS water resonance frequency in childhood brain tumours: a novel potential biomarker of temperature and tumour environment", *NMR Biomed*, vol. 27, no. 10, pp. 1222–1229, Oct. 2014.

[161] S. M. Sprinkhuizen et al., "Temperature dependence of the magnetic volume susceptibility of human breast fat tissue: an NMR study", *Magn. Reson. Mater. Physics, Biol. Med.*, vol. 25, no. 1, pp. 33–39, Apr. 2011.

[162] R. D. Peters and R. M. Henkelman, "Proton-resonance frequency shift MR thermometry is affected by changes in the electrical conductivity of tissue", *Magn. Reson. Med.*, vol. 43, no. 1, pp. 62–71, Jan. 2000.

[163] I. R. Young et al., "Modeling and observation of temperature changes in vivo using MRI", *Magn. Reson. Med.*, vol. 32, no. 3, pp. 358–369, Sep. 1994.

[164] J. Tazoe et al., "Brain core temperature of patients with mild traumatic brain injury as assessed by DWI-thermometry", *Neuroradiology*, vol. 56, no. 10, pp. 809–15, Oct. 2014.

[165] L. Kozak et al., “Using diffusion MRI for measuring the temperature of cerebrospinal fluid within the lateral ventricles”, *Acta Paediatr.*, vol. 99, no. 2, pp. 237–243, Feb. 2010.

[166] K. Sakai et al., “Age-dependent brain temperature decline assessed by diffusion-weighted imaging thermometry”, *NMR Biomed.*, vol. 24, no. 9, pp. 1063–7, Nov. 2011.

[167] K. Sakai, K. Yamada, and N. Sugimoto, “Calculation methods for ventricular diffusion-weighted imaging thermometry: phantom and volunteer studies”, *NMR Biomed.*, vol. 25, no. 2, pp. 340–6, Feb. 2012.

[168] E. Kardoulaki et al., “SNR in MI Catheter Receivers for MRI”, *IEEE Sens. J.*, Nov. 2015., doi: 10.1109/JSEN.2015.2500226.

[169] E. M. Kardoulaki et al., “Thin-film micro-coil detectors: Application in MR-thermometry”, *Sensors Actuators A Phys.*, vol. 226, pp. 48–58, May 2015.

[170] I. P. Wharton et al., “Design and development of a prototype endocavitary probe for high-intensity focused ultrasound delivery with integrated magnetic resonance imaging”, *J. Magn. Reson. Imaging*, vol. 25, no. 3, pp. 548–56, Mar. 2007.

[171] N. Todd et al., “Hybrid proton resonance frequency/T1 technique for simultaneous temperature monitoring in adipose and aqueous tissues”, *Magn. Reson. Med.*, vol. 69, no. 1, pp. 62–70, 2013.

[172] E. M. Kardoulaki et al., “Optothermal profile of an ablation catheter with integrated microcoil for MR-thermometry during Nd:YAG laser interstitial thermal therapies of the liver—an in-vitro experimental and theoretical study”, *Med. Phys.*, vol. 42, no. 3, pp. 1389–1397, 2015.

12,230 words, 66,687 characters